

Construction of Moisture-Stable Lithium Diffusion-Controlling Layer toward High Performance Dendrite-Free Lithium Anode

Jian Wang,* Huimin Hu, Shaorong Duan, Qingbo Xiao, Jing Zhang, Haitao Liu, Qi Kang, Lujie Jia, Jin Yang, Wenlong Xu, Huifang Fei, Shuang Cheng, Linge Li, Meinan Liu,* Hongzhen Lin,* and Yuegang Zhang*

Spatially random lithium nucleation and sluggish lithium diffusion across the electrode/electrolyte interface lead to uncontrollable lithium deposition and the growth of lithium dendrite on metallic lithium surface, causing severe safety problems. Herein, a functional rapid-ion-diffusion alloy layer on the metallic lithium surface (RIDAL-Li) is designed through a simple chemical reduction reaction. Such a layer efficiently reduces energy barriers for lithium transport and thus significantly homogenizes the lithium atom flux for lateral deposition, which are confirmed by electrochemical tests, theoretical simulations, and spectroscopic analysis. Furthermore, the as-prepared RIDAL layer also displays a much higher corrosion resistance to moisture and oxygen. As a result, in ether-based and carbonate-based electrolytes, the pretreated RIDAL-Li anode can achieve a long stripping/plating lifespan of 900 h and a high Coulombic efficiency of 99% without dendrite growth. Even after being exposed to the ambient environment with relative humidity of 51% for 60 min, the RIDAL-Li can survive for stripping/plating 400 h and exhibit a low overpotential of 18 mV, displaying the superiority for ambient atmosphere battery assembly. Matched with LiFePO_4 or sulfur cathode, the full cells exhibit remarkably improved stability and capacity retention, showing its suitability for applications in lithium metal batteries.

1. Introduction

With the development of modern intelligent society, high-energy-density lithium batteries become much more urgent owing to the emerge of smart devices and electrical vehicles.^[1] In comparison with conventional graphite anode (372 mA h g^{-1}), metallic lithium (Li) is considered to be the most ideal anode material for lithium batteries because of high theoretical specific capacity (3860 mA h g^{-1}) and relative low electrode potential (-3.04 V vs SHE).^[2–5] Unfortunately, the following issues challenged the utilization of metallic lithium anode: 1) the lithium dendrites growth on the lithium surface and the large volumetric changes during plating/stripping process; and 2) the crack of self-generated solid electrolyte interphase (SEI), resulting in depressed performance and lifespan.^[6,7] The uncontrollable lithium nucleation plating behaviors and sluggish lithium diffusion kinetics at the electrode/electrolyte interface are

J. Wang, H. Hu, J. Yang, S. Cheng, L. Li, M. Liu, H. Lin
i-Lab
Key laboratory of Multifunctional Nanomaterials and Smart Systems
Suzhou Institute of Nano-Tech and Nano-Bionics
Chinese Academy of Sciences
Suzhou 215123, China
E-mail: jian.wang@kit.edu; mnliu2013@sinano.ac.cn;
hzlin2010@sinano.ac.cn

J. Wang, H. Fei
Helmholtz Institute Ulm (HIU)
89081 Ulm, Germany

S. Duan, L. Jia, Y. Zhang
Department of Physics
Tsinghua University
Beijing 100084, China
E-mail: yuegang.zhang@tsinghua.edu.cn

 The ORCID identification number(s) for the author(s) of this article can be found under <https://doi.org/10.1002/adfm.202110468>.

© 2021 The Author(s). Advanced Functional Materials published by Wiley-VCH GmbH. This is an open access article under the terms of the Creative Commons Attribution License, which permits use, distribution and reproduction in any medium, provided the original work is properly cited.

DOI: 10.1002/adfm.202110468

Q. Xiao, W. Xu
Institute of Agricultural Resources and Environment
Jiangsu Academy of Agricultural Sciences
Nanjing 210014, China

J. Zhang
School of Materials Science and Engineering
Xi'an University of Technology
Xi'an 710048, China

H. Liu
Laboratory of Computational Physics
Institute of Applied Physics and Computational Mathematics
Beijing 100088, China

Q. Kang
Department of Polymer Science and Engineering
Shanghai Jiao Tong University
Shanghai 200240, China

M. Liu
Division of Nanomaterials and Jiangxi Key Lab of Carbonene Materials
Suzhou Institute of Nano-Tech and Nano-Bionics
Chinese Academy of Sciences
Nanchang 330200, China

responsible for the above challenges.^[8] The tardy interfacial lithium diffusion and the random lithium ionic flux cause large overpotential and low Coulombic efficiency (CE) under high current densities and hence limit the rate performance of lithium metal anode.^[9] For the large commercialization, the practical applications of lithium metal anodes are also limited by their critical assembly conditions ($O_2 < 1$ ppm; $H_2O < 1$ ppm) since it is sensitive to moisture and leads to side reactions.^[4]

Recently, numerous efforts have been put forward to resolve these challenges,^[2,10,11,12] including: in situ forming robust SEI by screening suitable electrolyte additives; fabricating 3D current collectors or matrix for accommodating preplated lithium and reserving space void for volumetric expansion; employing inorganic/organic (or polymer) artificial layers to suppress short-circuit by improving the SEI mechanic strength; and constructing lithium catalysis/modulation layer on the pristine Li. Among them, introducing alloying metal, that is, Si, Hg, In, or Zn to the lithium anode is deemed as a feasible way to increase the interfacial affinity to Li atoms, since the alloys can provide fast Li ion transportation channels.^[13] However, the addition of a large content of alloying metals into the lithium anode system will burden the integral battery with increasing weight, reducing energy density, and large volumetric change. A better choice is to construct a thin lithiophilic alloy layer on the lithium metal surface. Different from a typical passivation SEI layer which is electronic isolative and causes impedance to lithium-ion transport, the alloy layer allows fast diffusion of lithium ions and homogenous lithium ion/atom flux.^[14] Atomic layer deposition technology and polymer coating have been employed to improve the air/moisture stability of lithium metal.^[15] However, its high cost, the rather sophisticated process, and its poor ability to transport lithium ions hinder its large-scale application and further development. Note that most of the reported strategies are investigated in a selected electrolyte, while the feasibility of the alloy metal for universal applicability is still far from comprehensively understood.

Herein, a rapid-ion-diffusion alloy layer on metallic lithium surface (RIDAL-Li) is explored to modulate the lithium transport and plating behaviors for achieving dendrite-free lithium anodes. Via a chemical reaction between Li and liquid $SnCl_4$, Sn/Li_xSn alloy layer with a trace amount of insoluble LiCl is generated on the Li foil surface.^[12] Theoretical simulations and electrochemical analysis verify that such an alloy layer allows fast atom diffusion and uniform distribution of the lithium ions over the lateral plane, thus lower the interfacial transport impedance or barriers. Moreover, the pretreated lithium with RIDAL could tolerate the corrosion of electrolyte solvent and show the resistance in reacting with moisture, as unveiled by sum frequency generation spectroscopy (SFG). Therefore, the so-fabricated RIDAL SEI modified Li is capable of guiding initial lithium nucleation and successive lateral plating with lower potentials in carbonate or ether-based electrolytes. It yields a long plating/stripping cycling lifespan up to 900 h and an improved CE of 99% in the LiFSI-based electrolyte, showing significant advantages in prohibiting lithium dendrite growth. Even when being exposed to the tough practical moisture condition, the RIDAL-Li electrode is capable of resisting against the corrosion from oxygen and humid moisture and

exhibits low overpotentials of 18 mV. Matching with $LiFePO_4$ or sulfur cathode, the so-fabricated full cells exhibit remarkably improved stability and rate capacity, showing great promise for high energy density lithium metal batteries.

2. Results and Discussion

As is well known, the metallic Li is sensitive to the moisture and oxygen after being exposed to ambient surrounding, and it can also react with electrolyte/solvents to form solid depositions, which may lead to a rough surface, and thus deteriorates the performances of the lithium electrode (Figure 1A). An ideal metallic Li electrode should have the ability in resisting moisture and solvent corrosion. By introducing an artificial SEI layer on the metallic Li surface, the side reaction as mentioned above can be avoided and uniform lithium ion flux can be realized to deposit homogeneously (Figure 1B).^[4,5,7] In addition, the space charge theory proposed by Chazalviel suggests a higher uniform lithium diffusion rate may further suppress the growth of lithium dendrites. Therefore, how to construct a layer which not only protects Li away from moisture and electrolyte, but also propels lithium ion diffusion easily seems very important and challenging. To achieve the above goal, the diffusion rate of lithium atoms in a series of lithium salts were compared and evaluated. A wide-area diffusion path with the lowest global diffusion energy barrier for the diffusion of lithium ions was found.^[16] As shown in Figure 1C–L and Figure S1, Supporting Information, two types diffusion modes, that is, interstitial diffusion and vacancy diffusion for lithium atom were well-investigated in all systems. LiF is a well-known byproduct derived from electrolyte and protects the lithium surface. The insoluble LiCl is also well-known wide-band-gap insulator with the band gap of 6.27 eV in our calculations (Figure 1J). Compared with LiF, the interstitial diffusion of Li ions is still favorable mode in LiCl bulk, but the diffusion barrier is significantly decreased from 0.44 to 0.33 eV.^[17] Therefore, the formation of insoluble LiCl can facilitate and accelerate lithium-ion transport across the interface.^[18] As a demo, a typical metal of Sn is selected as the lithium ion flux modulator in here. First, the various stable crystal phase structures including LiF, LiCl, Sn, LiSn, and $Li_{13}Sn_5$ were optimized (Table S1, Supporting Information). Introducing the metallic alloy into the system (Figure 1E–G), the interstitial lithium ion diffusion is propelled owing to the unique structure of Sn, and it only exhibited extremely low diffusion energy barrier (0.08 eV), as displayed in Figure 1K. With the increasing lithium concentration in Li–Sn alloy, the favorable diffusion mode may be changed and the diffusion barrier is slightly increased to 0.19 eV (Figure S1, Supporting Information). Hence synergetic interaction between LiCl and Li–Sn alloy could improve the lithium-ion transport through the SEI. A more uniform lithium deposition at the SEI/Li interface is anticipated and the formation of lithium dendrite is believed to be inhibited. Meanwhile, the capability of moisture on the metallic Li and alloy surface is also investigated, as displayed in Figure 1H–I and Figure S2, Supporting Information. The water molecular is more preferential to the metallic Li surface since it can react with active Li, disturbing the surface stability. In contrast, the adsorption energy is reduced to 0.45 eV

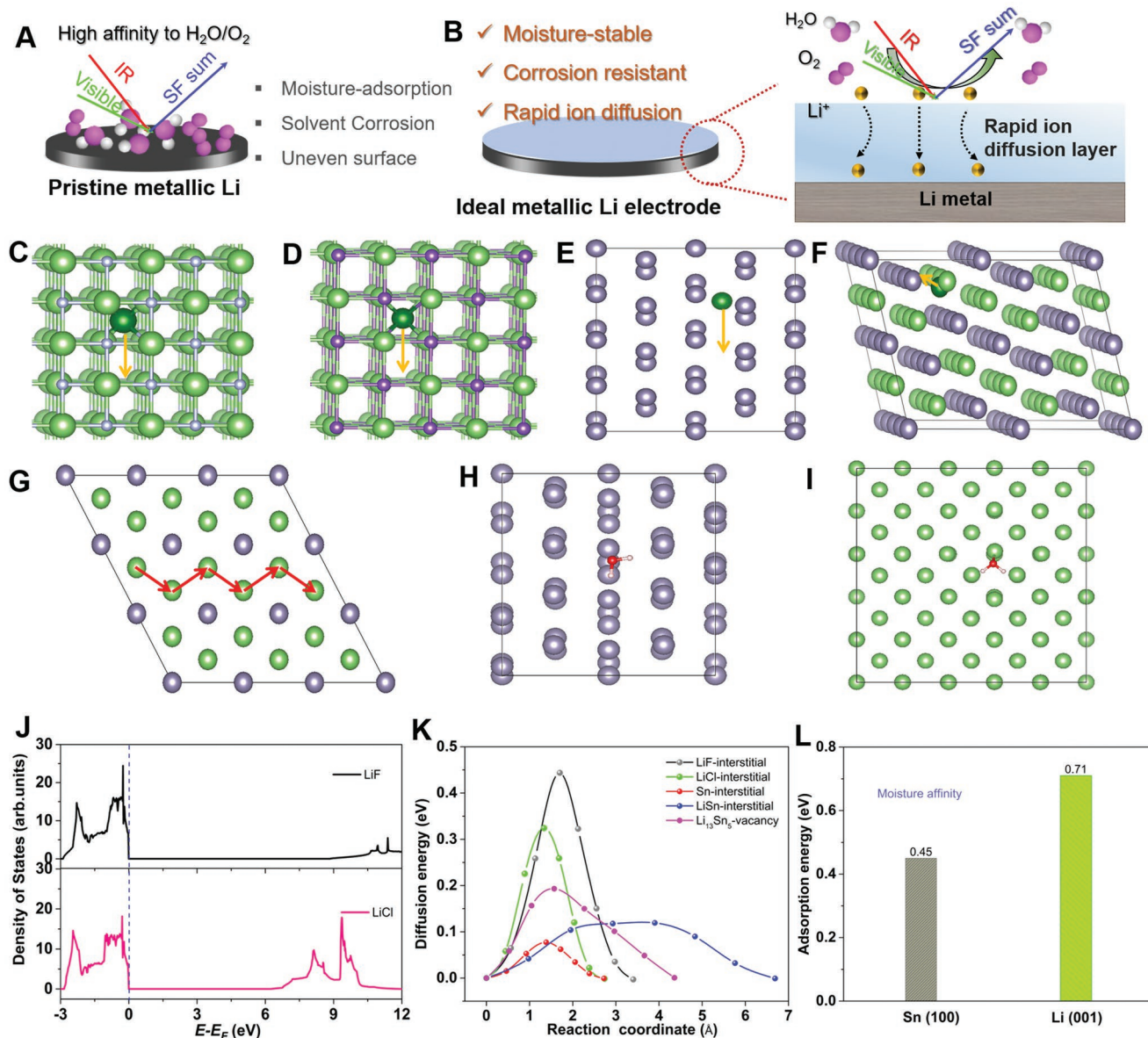


Figure 1. Schematic illustration of moisture and oxygen on A) pristine Li surface and B) ideal metallic Li surface; Atomic structures of interstitial Li-ion diffusion in C) LiF, D) LiCl, E) Sn, and F) LiSn; The yellow arrow indicates the diffusion direction of the interstitial Li. G) Atomic structure of vacancy Li-ion diffusion in $\text{Li}_{13}\text{Sn}_5$; Water moisture molecule adsorbed on H) Sn(100) surface and I) Li(001) surface. The red arrow indicates the trajectory of Li vacancy from the initial state to the final state. J) The comparison of electronic density of states between LiF and LiCl; K) The summary of the Li ion diffusion energies in various materials; L) The adsorption energies of H_2O on Sn (100) and Li (001) surface. The dark green, green, silver, purple, gray, red, and light pink balls represent interstitial Li, Li, F, Cl, Sn, O, and H atoms, respectively.

upon the moisture water reaches the alloy surface, showing the rather chemical stability.

Following above guideline, the metal precursor (SnCl_4) is dissolved in dimethyl ether (DME) and then dip-coated on metallic lithium surface, spontaneously yielding the Sn/ Li_xSn alloy layer via chemical reduction of Sn(IV) by lithium. As shown in the scanning electronic microscopy (SEM) images (Figure 2A), compared with pristine Li metal (Figure S3, Supporting Information), large numbers of uniformly distributed nanoparticles were observed on the lithium surface after self-reaction. Further, the thickness of the so-formed RIDAL layer

is characterized to be about $7 \mu\text{m}$ in average according to the cross-sectional SEM image (Figure 2B). Both the corresponding surface and cross-sectional SEM energy dispersed spectroscopy mappings confirm the presence and uniform distribution of elemental Sn and Cl in the formed RIDAL SEI layer (Figure 2A,B). Both the RIDAL-Li and pristine Li show the typical crystal peaks of metallic Li. RIDAL-Li shows distinct feature peaks at 35° and 51° attributed to metallic Sn in the X-ray diffraction patterns (Figure 2C). An extra peak at 38° is observed, suggesting the formation of lithiated Sn alloys ($\text{Li}_{13}\text{Sn}_5$) on the metallic lithium surface. As displayed in the high-resolution

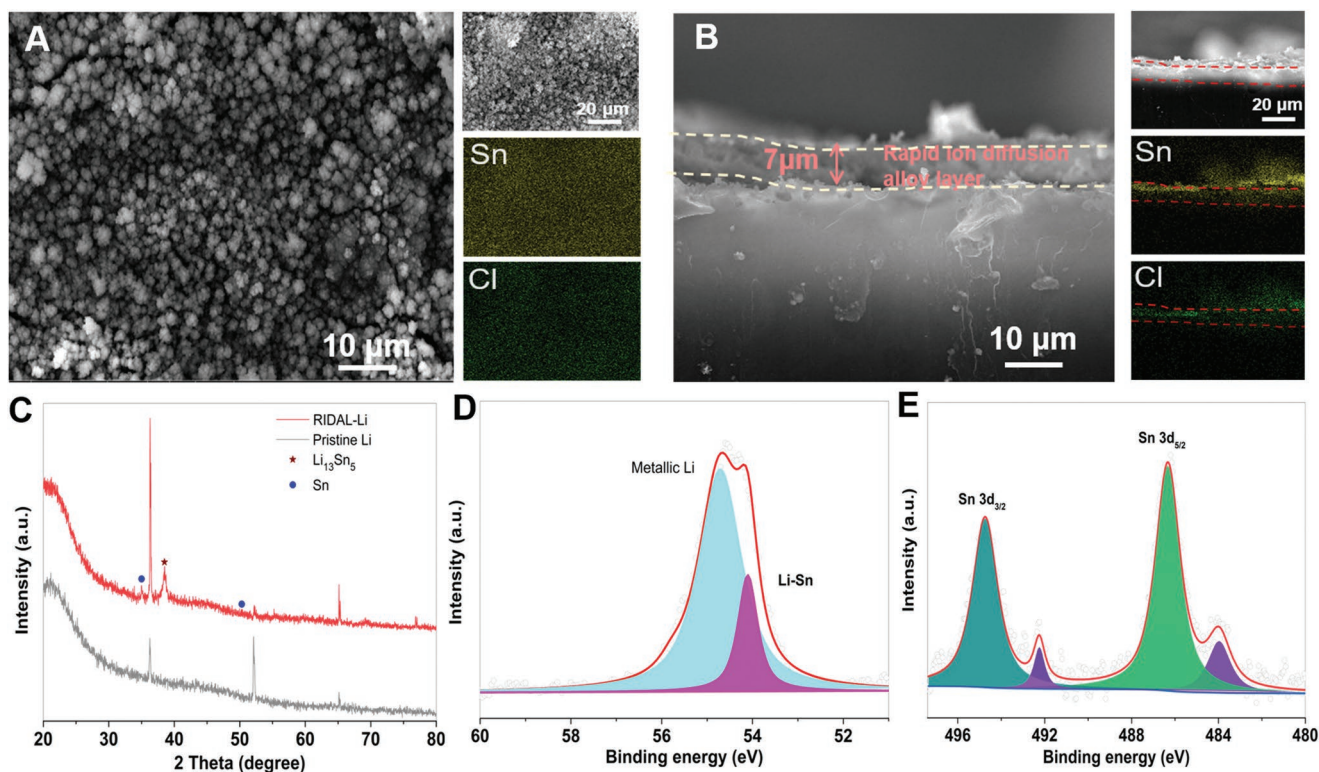


Figure 2. A) The SEM image and EDS elemental mappings of rapid ion diffusion alloy layer on lithium surface by self-reacted dip-coating. B) The cross-sectional SEM image and EDS elemental mappings of RIDAL-Li, showing the thickness of RIDAL is about 7 μm . C) X-ray diffraction (XRD) pattern of RIDAL-Li and pristine Li. The high-resolution XPS spectra of D) Li 1s and E) Sn 3d in the RIDAL-Li electrode surface.

Li 1s X-ray photoelectronic spectroscopy (XPS) spectrum in Figure 2D and Figure S4A, Supporting Information, the characteristic peak at 54.7 eV is assigned to the metallic Li, while a new fitting peak centered at 54.1 eV ascribed to the Li–Sn bond comes out, suggesting the formation of Li_xSn alloy. In the high-resolution Sn 3d spectrum (Figure 2E), the Sn $3d_{5/2}$ at 494.5 eV and Sn $3d_{3/2}$ peaks at 486.1 eV are able to be detected on the surface of pretreated sample.^[12,19] The presence of LiCl in the RIDAL SEI layer is evidenced by its characteristic signal at 199.8 eV in the Cl 2p spectrum (Figure S4B, Supporting Information).

To illustrate the modulation effect of the RIDAL layer, symmetric and asymmetric cells based on RIDAL-Li and pristine Li were assembled in carbonate and ether electrolytes, respectively. As shown in the electrochemical impedance spectroscopy, the RIDAL-Li electrode displays one charge transfer process and a lithium ion transfer process. And the pretreated RIDAL-Li electrode keeps the smaller charge transfer resistance than the pristine Li one (2.07 vs 15.35 Ω), indicating the highly conductive electrode/electrolyte interface (Figure S5, Supporting Information).^[20] Compared with the stable resistances of the RIDAL-Li electrode, the resistance of the pristine Li becomes smaller gradually in the successive cycles, which might be caused by the formation of in situ generated SEI layer (Figure S5, Supporting Information).^[21] As shown in Figure 3A, the RIDAL-Li electrode has a smaller slope (1.590) than that of pristine Li (1.847), implying the fast ionic transport across the preformed alloy SEI layer.^[20,22] Besides, as shown in

Figure 3B and Figure S6, Supporting Information, the lithium ion transference number of the cell based on RIDAL-Li electrode is calculated to be 0.548, which is higher than that of the cell based on pristine Li.^[23] These results co-reveal the ionic transport across the interface and in the alloy interior are significantly improved, realizing a smooth deposition of Li. The ability of the RIDAL SEI in decreasing the nucleation and transport barriers is also reflected in the lifespans and CEs in different electrolytes under the plating/stripping capacity of 1 mA h cm^{-2} . Figure 3C and Figure S7, Supporting Information show the voltage curves of the cells based on pristine Li and RIDAL-Li at 1 mA cm^{-2} in various electrolytes. In the conventional carbonate-based electrolyte, the pretreated RIDAL-Li electrode exhibits a long life of 200 h within an overpotential of 80 mV, while the pristine Li shows a depressed lifespan of 80 h and large fluctuating overpotentials (usually above 2000 mV). Similarly, in the ether-based electrolytes, the symmetric cells based on RIDAL-Li electrodes display enhanced cycle stability and low overpotentials, significantly better than that of pristine Li electrodes (Figure S7, Supporting Information). Note that in the LiFSI-based ether electrolyte, the performances of symmetric cells are superior to that in LiTFSI and LiPF₆-based ones. A longer life of about 650 h with a stable overpotential of 30 mV is achieved at 1 mA cm^{-2} , demonstrating the advantages of the preformed RIDAL SEI layer. As a contrast, the pristine Li electrode displays a fluctuated voltage curve in the successive plating/stripping process and then encounters a sudden voltage drop, indicating the formation of lithium dendrite.^[24]

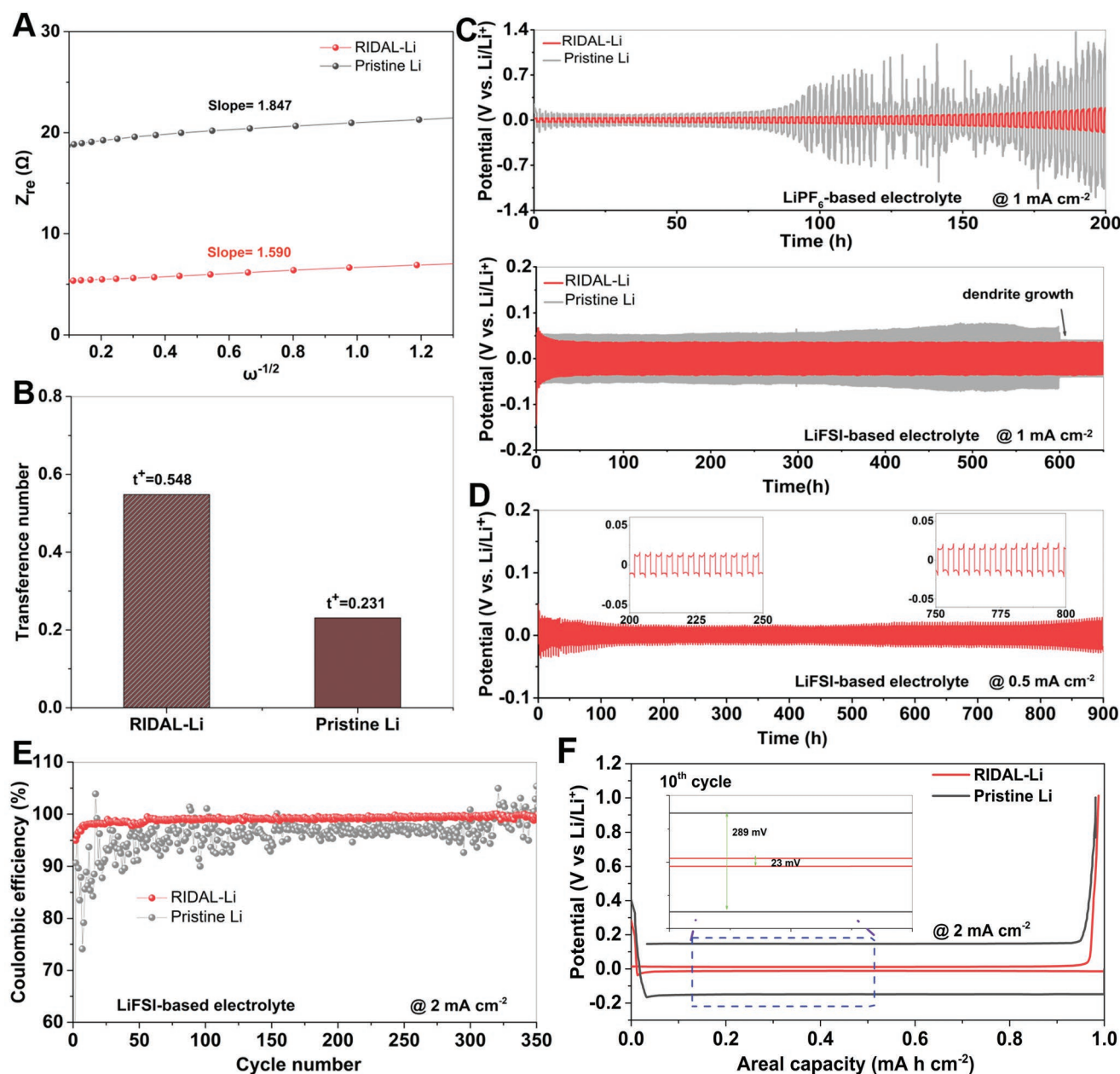


Figure 3. A) Plot of impedance as a function of the inverse square root of the angular frequency (ω) at low frequency. B) The transference number of RIDAL-Li and pristine Li electrodes. C) Galvanostatic plating/stripping stability of the symmetric cells based on RIDAL-Li and pristine Li electrodes at current density of 1 mA cm^{-2} in ether- or carbonate-based electrolytes D) Long plating/stripping stability of the symmetric cell based on RIDAL-Li electrode at 0.5 mA cm^{-2} . E) The Coulombic efficiency measurement of asymmetric cells based on RIDAL-Li and pristine Li electrodes at 2 mA cm^{-2} . F) The corresponding potential profiles at the tenth cycle at the current density of 2 mA cm^{-2} .

Reducing the current density to a lower density of 0.5 mA cm^{-2} (Figure 3D), the RIDAL-Li electrode keeps quite stable overpotential tendency and runs for a lifespan up to 900 h. Similar stable overpotential and low diffusion barrier results are also achieved at high current densities (Figures S8 and S9, Supporting Information).

In order to further evaluate the functions of the rapid ion diffusion modulation layer, the asymmetric Li–Cu cells based on the pristine copper with RIDAL-Li or pristine Li were assembled, respectively. As is well known, the CE is capable

of witnessing the stability of the artificial SEI layer, which is defined as the stripping lithium amount divided by the plating lithium amount.^[11,25] The initially plated lithium atoms are stripped off from the copper electrode and then deposited onto the lithium electrode during the charging process, and the depositing morphology substantially affects the lithium ion flux distribution in the successive discharging half cycle, and hence influences the lithium plating behaviors on the copper side. In the optimized FSI-based ether electrolyte, along with cycling, the CE values of the Li–Cu cell based on pristine Li

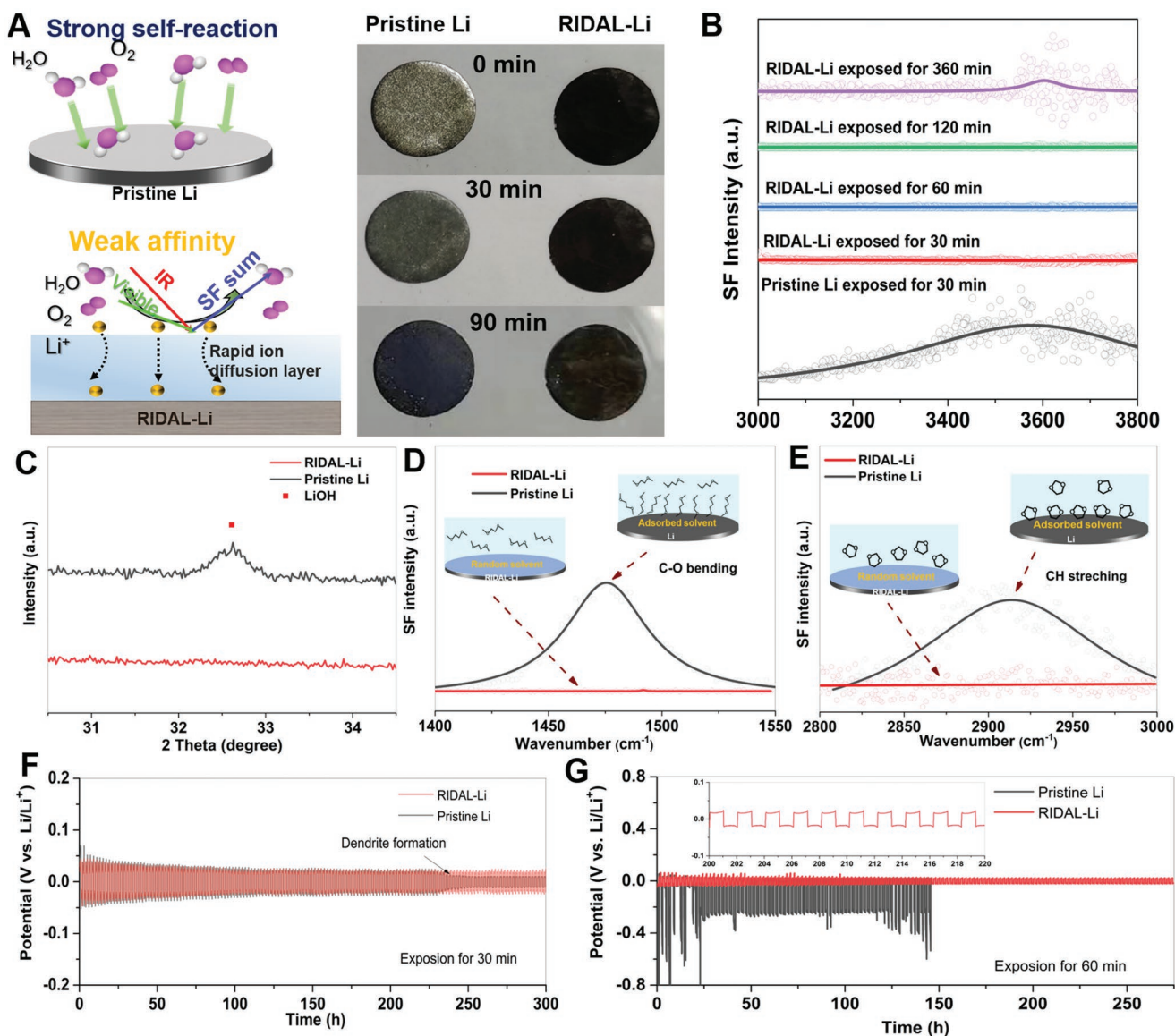


Figure 4. A) The optical image evolution of these two lithium foils exposed to humid air of 44% for 0, 30, and 90 min. B) The SFG spectra evolution of these two lithium foils exposed to humid surrounding, indicating moisture tends to adsorb on pristine Li. C) Corresponding XRD pattern of RIDAL-Li and pristine Li exposed to air after 3 h. SFG spectra comparison of the two lithium electrodes in D) DME/electrode interface and E) DOL/electrode interface, respectively. Galvanostatic plating/stripping stability of the symmetric cells based on exposed RIDAL-Li and pristine Li electrodes F) for 30 min and G) for 60 min in the ambient humid surroundings, respectively.

electrode undergo up-and-down and display a decreased tendency after 300 cycles at 2 mA cm⁻², indicating the dendrite growth of lithium at high-rate ionic flux. In contrast, the pre-treated RIDAL-Li electrode maintains stable CE values above 99% after the initial lithiation of alloy and stabilizes for more than 350 cycles (Figure 3E). The similar stable phenomena can also be observed when decreasing the current density to 1 mA cm⁻² (Figure S10, Supporting Information). As displayed in Figure 3F, the pretreated RIDAL-Li electrodes show the lower overpotentials, indicating the decreased barriers and increased ion conductivity upon introducing the artificial alloy layer. Moreover, the RIDAL-Li electrode remains the superior CE and lifespan in the LiTFSI-based and LiPF₆-based electrolyte

system, as displayed in Figures S11 and S12, Supporting Information. These results demonstrate that the alloy layer on the Li surface can propel the lithium ion transport across the interface and interior and suppress the side reaction between the metallic Li and the electrolyte during cycling.

To pursue the large production in industrial field, the corrosion of moisture and solvents are tough challenges deserved to be resolved since the metallic Li is sensitive to moisture and could not be stable in the ambient moisture surrounding (Figure 4A).^[15] Figure 4A and Figure S13, Supporting Information depict and display the optical images of pristine Li and RIDAL-Li electrodes exposed to practical environment with the humidity of 44% at room temperature (Figure S13,

Supporting Information). With the increase of exposed time, the pristine Li without any protection was shining at the beginning and became gray then to dark gray, suggesting the side reaction formed on the surface. However, in big contrast, no obvious color change was observed in the RIDAL-Li, implying its superior stability in the humid surrounding. The top view and cross-sectional SEM images of these two lithium foils were also obtained. As shown in Figure S14, Supporting Information, after reacting with the moisture, the surface became rougher and the thickness was increased. The corrosive layer on the pristine Li became much rougher and contained many collapsed structures. In sharp contrast, the RIDAL-Li electrode remained the original surface morphology composed of well-distributed Sn nanoparticles along with the increasing of exposure time. The moisture affinity adsorbed on the metallic Li surface was studied by interfacial vibrational SFG spectroscopy at electrode/air interface.^[26] As displayed in Figure 4B, the pristine Li one shows the feature peaks attributed to water and extensive affinity to the moisture adsorption at the interface after exposing to humid surrounding for 30 min. However, the RIDAL-decorated Li shows the resistance to the moisture and no feature SFG peaks were observed even after exposing for 120 min. To clearly figure out the formed substance on metallic lithium surface, as displayed in Figure 4C and Figure S15, Supporting Information, pristine Li without RIDAL SEI layer shows a feature diffraction peak at 32.6°, which is attributed to the LiOH resulted from the reaction between lithium metal and oxygen/moisture in the air. The absence of LiOH in RIDAL-Li electrode means that the artificial RIDAL SEI layer can effectively keep stable in humid surrounding and inhibit the moisture reaction. Such surface protection ability is also reflected in the resistance to the electrolyte solvents. As displayed in Figure 4D,E, in the SFG spectroscopy, the signals at 1475 cm⁻¹ are assigned to C–O bending vibration signals of DME, respectively.^[27] The stronger intensity of C–O signal on pristine Li surface than that on RIDAL-Li demonstrates that the DME molecules have high affinity to pristine Li surface and almost little amount on the preformed SEI layer. Regarding the solvent of DOL, the similar phenomenon is obtained (Figure 4E), strongly showing the high resistance of the SEI layer to the solvent in the electrolyte. The less coordinated solvent with lithium ions means the low desolvation energy barrier to overcome on the interface, so that the bare lithium ion can easily reach the metallic surface, realizing a fast-rapid transport. From the practical view, the symmetric cells based on the exposed Li electrodes are also tested. As shown in Figure 4F,G, exposed to the humidity of 51%, the exposed RIDAL-Li electrode keeps the similar behaviors without any dendrite formation. Increasing the exposed time up to 60 min, the pristine Li exhibits extremely worse electrochemical plating/stripping behaviors and the cell is nearly unable to work (Figure 4G). While, the RIDAL-Li electrode can last for 400 h with the low stable overpotential of 18 mV at 1 mA cm⁻², significantly implying the stability of RIDAL SEI under ambient humid surrounding. As illustrated, very few reports have investigated the stability in a practical moisture environment and the RIDAL-Li electrode displays the excellent lifespan. (Table S2, Supporting Information).

To deep clarify the RIDAL SEI, ex situ SEM and XPS were conducted to observe the cycled surface. As shown in Figure 5A,

the RIDAL-Li still reserved many nanoparticles without aggregation after 50 cycles, indicating the possibility of uniform lithium ion transport across the artificial SEI layer. However, the pristine Li without any protection exhibits many deep pits and large aggregation, resulting in formation/deformation of SEI layers under inhomogeneous stress (Figure 5B). In the cross-sectional SEM image, in comparison with the thickness in Figure 2B, the thickness of the cycled SEI layer increases slightly (7 vs 10 μm), which might be ascribed to partial volumetric change and the formation of LiF derived from LiFSI (Figure 5C). To further make sense this, the new coming elemental fluorine was detected in the surface and cross-section and it is also uniformly distributed on the surface and cross-section (Figure 5D). The surface composition of RIDAL-Li electrodes after cycling were also studied by XPS measurements, as shown in Figure 5E,F and Figure S16, Supporting Information. In the high-resolution Li 1s spectrum (Figure 5E), both the peaks assigned to metallic Li and Li–Sn can be observed, which are consistent with the SEM results. A new peak at 56.0 eV comes out, which is attributed to the formation of LiF. Meanwhile, the Li–F bond (685.0 eV) is also verified in the high-resolution F 1s spectrum (Figure 5F), demonstrating the formation of inorganic LiF on metallic Li surface during the cycle. To investigate the RIDAL layer from the 3D structure distribution, the unique time-of-flight second ion mass spectrometry (TOF-SIMS) was carried out to observe the distribution and depth information of each species (Figure 5G,H). Figure 5G displayed reconstructed images from the overlay to each species. Both the surface and overlay morphology display a smooth ionic distribution. Obviously, the electrochemically formed LiF is on the top of the RIDAL layer (Figure 5H). And the Li species have an overlap with the Sn, indicating the fast lithium diffusion in the Sn alloy layer. From the above theoretical simulation, electrochemical and morphological results, the functions of rapid ion diffusion alloyed layer in modulating lithium nucleation are well illustrated (Figure 5I,J). According to the SFG results, organic solvent of electrolytes can be absorbed on the surface of pristine Li foils (Figure 5I). The adsorbed electrolyte solvent would increase the energy barrier to desolvate and result in an unstable interface with a great deal of defects such as pits, humps, and cracks, leading to a huge lithium nucleation barrier. In the following plating process, the unsmooth surface will trigger the dendrite growth under the inhomogeneous Li ion flux. While for RIDAL-Li, as-prepared RIDAL SEI layer could understand high resistance toward electrolyte solvent by SFG results (Figure 5J), decreasing the desolvation barrier. Owing to the self-reaction between Li and Sn, the surface of lithium foils would be smoother. The as-fabricated alloy layer allows fast Li ion diffusion from the interface to interior, which efficiently reduces the energy barriers for lithium transport, nucleation, and plating. Through the RIDAL SEI layer, the plating behaviors of lithium atom flux was uniformized before reaching the below metallic lithium, resulting in smooth deposition of lithium. In the successive cycling, the plating lithium atom is evenly distributed on the formed surface without any dendrite growth. Therefore, the stability and lifespan of cells are significantly improved under the regulation of the RIDAL layer.

In order to further explore the advantages in practical application of RIDAL-Li electrode, the cycling performances of Li–S

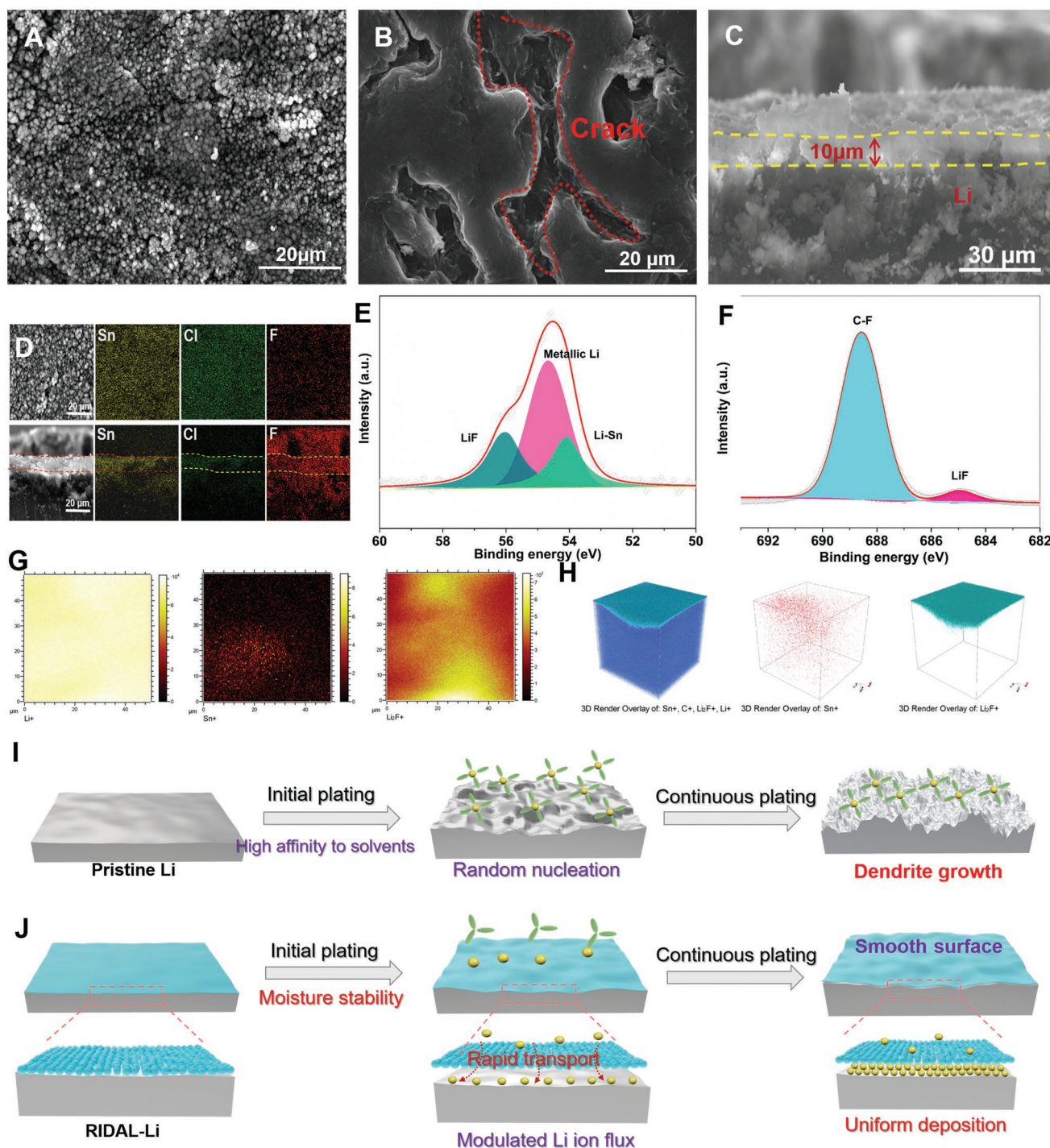


Figure 5. The top view SEM images of A) RIDAL-Li, B) pristine Li, and C) the cross-sectional SEM images of RIDAL-Li after 50 cycles in the LiFSI-based electrolyte at 1 mA cm^{-2} . D) The corresponding EDS elemental mappings of RIDAL-Li after cycling. The high-resolution XPS spectra of E) Li 1s and F) F 1s of RIDAL-Li after cycling. G) The TOF-SIMS color mappings of elemental Li⁺, Sn⁺, and Li₂F⁺ species. H) The 3D reconstruction of the overlay; Sn⁺ and Li₂F⁺. The schematic illustration of plated lithium behaviors on I) pristine Li and J) RIDAL-Li at the beginning or in the successive cycle.

and Li–LiFePO₄ full cells are evaluated. When paired with a commercial LiFePO₄ cathode (Figure 6A), the full cells based on RIDAL-Li electrodes consistently exhibit a much better rate capability compared with pristine Li electrodes. The cells based on pretreated RIDAL-Li deliver capacities of 128 and

106 mA h g⁻¹ at high rates of 2 and 5 C (1 C = 170 mA g⁻¹), respectively, which are higher than that of pristine ones (120 vs 93 mA h g⁻¹). The cycling performance of Li–LiFePO₄ full cells cycled at 1 C shown in Figure 6B. The full cells based on pristine Li electrodes exhibit rapid capacity decay, and the capacity

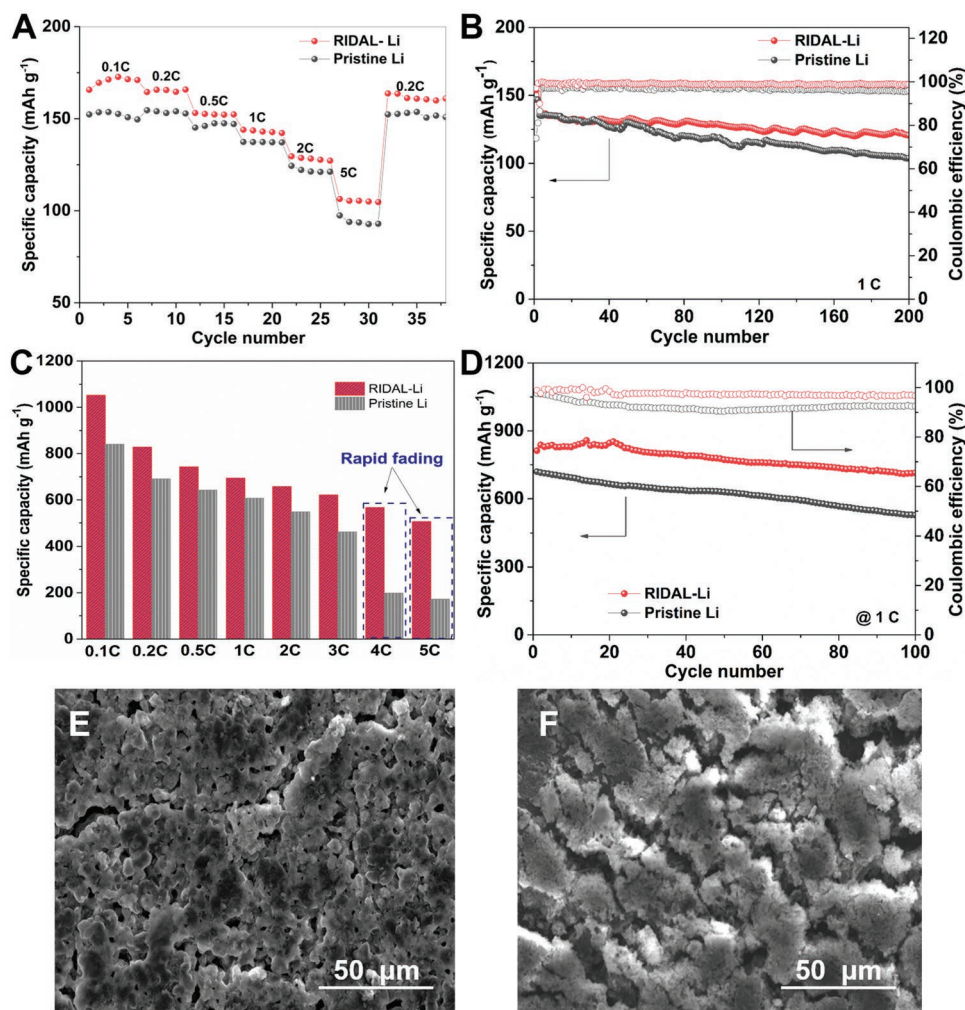


Figure 6. A) Rate performance and B) cycling stability of Li–LiFePO₄ full cells based on RIDAL-Li electrode and pristine Li electrode. C) Rate performance and D) cycling stability of Li–S batteries based on RIDAL-Li electrode and pristine Li electrode. The ex situ SEM images of the E) RIDAL-Li and F) pristine Li after cycling.

retention rate after 200 cycles is only 76.8%. In contrast, the full cells based on the RIDAL-Li electrodes deliver excellent cycling stability and still maintain 121 mA h g⁻¹ with the capacity retention of 89.2% after 200 cycles. The slight fluctuation of the full cells might be ascribed to temperature fluctuation from the daytime to the night. What should be pointed out is that the CE of the cell based on RIDAL-Li is significantly improved compared with the pristine Li one. Furthermore, Figure 6C and Figure S17, Supporting Information show the cycling performance of full cells at different current rates. In comparison with the cell based on pristine Li, the achieved high performance of the full cell based on RIDAL-Li at high rates, that is, 4 and 5 C strongly demonstrates the feasibility of the rapid ionic diffusion across the electrode/electrolyte interface. As depicted in Figure 6D, the full cell based on RIDAL-Li electrode delivers an initial discharge capacity of 714 mA h g⁻¹ with the capacity retention of 85.2% after 100 cycles, whereas the full cell based on pristine Li electrode has a lower capacity and rapid capacity fading. These results demonstrate that the RIDAL-Li can significantly improve the capacity retention rate and rate

performance of the full cells, and it will have excellent prospects in actual applications. After cycling, the surface morphologies of two full cells were characterized (Figure 6E,F and Figure S18, Supporting Information). The RIDAL-Li electrode remains a smooth surface composed of many nanoparticles without obvious dendrites, while pristine Li surface is quite porous with the dendrite growth and collapse. It is roughly estimated that the volume expansion ratio of the cycled pristine Li electrode including dead Li is much higher than that in RIDAL-Li electrode (3.56% vs 1.1%) in comparison to the 450 μm of commercial Li foil one (Figures S19 and S20, Supporting Information).

3. Conclusion

In summary, a lithophilic alloy layer affording rapid interfacial Li ion diffusion kinetics is chemically fabricated on lithium foil surface. Such a layer efficiently reduces the energy barriers against interfacial lithium transportation, decreases the surface affinity to the solvent molecules, and significantly homogenizes

the lithium atom flux for lateral deposition, as thoroughly unveiled by spectroscopic measurements, theoretical simulations, and electrochemical analysis. As a consequence, the pretreated lithium electrode exhibits a low overpotential of 30 mV, and a long lifespan of more than 650 h at 1 mA cm⁻², and an improved CE of 99% without dendrite formation in the LiFSI-based electrolyte. Moreover, exposed under a realistic surrounding with moisture humidity of 51%, the symmetric cell remains a low overpotential of 18 mV for stripping/plating 400 h. The so-assembled Li–S and Li–LiFePO₄ full cells based on pretreated RIDAL-Li electrodes show higher capacity and rate performance, demonstrating the great promise for future commercialization.

Supporting Information

Supporting Information is available from the Wiley Online Library or from the author.

Acknowledgements

J.W., H.H., S.D., and Q.X. contributed equally to this work. J.W. thanks the funding support provided by the Germany Alexander von Humboldt Foundation Fellowship and the Innovative and Entrepreneurial Doctor in Jiangsu Province. This work is funded by the Jiangsu Province Natural Science Foundation (No. BK20210130), the National Natural Science Foundation of China (Nos. 21773294, 21972164, 22078136, 22075313), the Science and Technology Project of Jiangxi Province (20192BCB23028), and Jiangxi Double Thousand Talent Program (JXSQ2019101072). The authors thank for technical support from Nano-X, Suzhou Institute of Nano-tech and Nano-bionics, Chinese Academy of Sciences.

Conflict of Interest

The authors declare no conflict of interest.

Data Availability Statement

The data that support the findings of this study are available from the corresponding author upon reasonable request.

Keywords

dendrite-free lithium anodes, lithium alloy layers, lithium metal batteries, moisture stability, rapid ion diffusion

Received: October 15, 2021

Revised: November 11, 2021

Published online: December 1, 2021

- [1] a) J. Wang, L. Jia, H. Lin, Y. Zhang, *ChemSusChem* **2020**, *13*, 3404; b) J. Zhi, S. Li, M. Han, P. Chen, *Sci. Adv.* **2020**, *6*, eabb1342; c) G. Zhou, L. Xu, G. Hu, L. Mai, Y. Cui, *Chem. Rev.* **2019**, *119*, 11042; d) J. Wang, L. Jia, J. Zhong, Q. Xiao, C. Wang, K. Zang, H. Liu,

- H. Zheng, J. Luo, J. Yang, H. Fan, W. Duan, Y. Wu, H. Lin, Y. Zhang, *Energy Storage Mater.* **2019**, *18*, 246.
 [2] C. Z. Sun, Y. D. Ruan, W. P. Zha, W. W. Li, M. L. Cai, Z. Y. Wen, *Mater. Horiz.* **2020**, *7*, 1667.
 [3] a) R. Xu, Y. Xiao, R. Zhang, X. B. Cheng, C. Z. Zhao, X. Q. Zhang, C. Yan, Q. Zhang, J. Q. Huang, *Adv. Mater.* **2019**, *31*, 1808932; b) P. Albertus, S. Babinec, S. Litzelman, A. Newman, *Nat. Energy* **2018**, *3*, 16; c) F. Duffner, N. Kronemeyer, J. Tubke, J. Leker, M. Winter, R. Schmich, *Nat. Energy* **2021**, *6*, 123.
 [4] J. Wang, J. Yang, Q. Xiao, J. Zhang, T. Li, L. Jia, Z. Wang, S. Cheng, L. Li, M. Liu, H. Liu, H. Lin, Y. Zhang, *Adv. Funct. Mater.* **2021**, *31*, 2007434.
 [5] J. Wang, J. Zhang, S. Cheng, J. Yang, Y. Xi, X. Hou, Q. Xiao, H. Lin, *Nano Lett.* **2021**, *21*, 3245.
 [6] a) Y. D. Liu, Q. Liu, L. Xin, Y. Z. Liu, F. Yang, E. A. Stach, J. Xie, *Nat. Energy* **2017**, *2*, 17083; b) J. Qian, W. A. Henderson, W. Xu, P. Bhattacharya, M. Engelhard, O. Borodin, J. G. Zhang, *Nat. Commun.* **2015**, *6*, 6362; c) X.-R. Chen, Y.-X. Yao, C. Yan, R. Zhang, X.-B. Cheng, Q. Zhang, *Angew. Chem. Int. Ed.* **2020**, *59*, 7743; d) J. Wang, J. Zhang, S. Duan, T. Li, L. Jia, H. Liu, L. Li, S. Cheng, H. Hu, M. Huang, H. Hu, S. Zhang, Q. Xiao, H. Lin, *Chem. Eng. J.* **2021**, *429*, 132352.
 [7] J. Zhang, C. You, H. Lin, J. Wang, *Energy Environ. Mater.* **2021**, <https://doi.org/10.1002/EEM2.12250>.
 [8] a) Y. Zhang, C. Wang, G. Pastel, Y. Kuang, H. Xie, Y. Li, B. Liu, W. Luo, C. Chen, L. Hu, *Adv. Energy Mater.* **2018**, *8*, 1800635; b) L. Li, M. Wang, J. Wang, F. Ye, S. Wang, Y. Xu, J. Liu, G. Xu, Y. Zhang, Y. Zhang, C. Yan, N. V. Medhekar, M. Liu, Y. Zhang, *J. Mater. Chem. A* **2020**, *8*, 8033; c) S. Li, L. Fan, Y. Lu, *Energy Storage Mater.* **2019**, *18*, 205.
 [9] a) J. Wang, L. Jia, H. Liu, C. Wang, J. Zhong, Q. Xiao, J. Yang, S. Duan, K. Feng, N. Liu, W. Duan, H. Lin, Y. Zhang, *ACS Appl. Mater. Interfaces* **2020**, *12*, 12727; b) L. Peng, Z. Wei, C. Wan, J. Li, Z. Chen, D. Zhu, D. Baumann, H. Liu, C. S. Allen, X. Xu, A. I. Kirkland, I. Shakir, Z. Almutairi, S. Tolbert, B. Dunn, Y. Huang, P. Sautet, X. Duan, *Nat. Catal.* **2020**, *3*, 762.
 [10] a) Z. Y. Tu, S. Choudhury, M. J. Zachman, S. Y. Wei, K. H. Zhang, L. F. Kourkoutis, L. A. Archer, *Joule* **2017**, *1*, 394; b) R. Xu, X.-B. Cheng, C. Yan, X.-Q. Zhang, Y. Xiao, C.-Z. Zhao, J.-Q. Huang, Q. Zhang, *Matter* **2019**, *1*, 317; c) F. Wu, Y.-X. Yuan, X.-B. Cheng, Y. Bai, Y. Li, C. Wu, Q. Zhang, *Energy Storage Mater.* **2018**, *15*, 148; d) S. J. Park, J. Y. Hwang, C. S. Yoon, H. G. Jung, Y. K. Sun, *ACS Appl. Mater. Interfaces* **2018**, *10*, 17985; e) J. M. Zheng, M. H. Engelhard, D. H. Mei, S. H. Jiao, B. J. Polzin, J. G. Zhang, W. Xu, *Nat. Energy* **2017**, *2*, 17012; f) F. Pei, A. Fu, W. Ye, J. Peng, X. Fang, M.-S. Wang, N. Zheng, *ACS Nano* **2019**, *13*, 8337; g) J. Xie, J. Wang, H. R. Lee, K. Yan, Y. Li, F. Shi, W. Huang, A. Pei, G. Chen, R. Subbaraman, J. Christensen, Y. Cui, *Sci. Adv.* **2018**, *4*, eaas9820; h) Y. Gao, Z. Yan, J. L. Gray, X. He, D. Wang, T. Chen, Q. Huang, Y. C. Li, H. Wang, S. H. Kim, T. E. Mallouk, D. Wang, *Nat. Mater.* **2019**, *18*, 384.
 [11] J. Gu, Q. Zhu, Y. Shi, H. Chen, D. Zhang, Z. Du, S. Yang, *ACS Nano* **2020**, *14*, 891.
 [12] J. Wang, J. Yang, Q. Xiao, L. Jia, H. Lin, Y. Zhang, *ACS Appl. Mater. Interfaces* **2019**, *11*, 30500.
 [13] a) W. Tang, X. S. Yin, S. J. Kang, Z. X. Chen, B. B. Tian, S. L. Teo, X. W. Wang, X. Chi, K. P. Loh, H. W. Lee, G. W. Zheng, *Adv. Mater.* **2018**, *30*, 1801745; b) G. He, Q. W. Li, Y. L. Shen, Y. Ding, *Angew. Chem. Int. Ed.* **2019**, *58*, 18466; c) X. Liang, Q. Pang, I. R. Kochetkov, M. S. Sempere, H. Huang, X. Q. Sun, L. F. Nazar, *Nat. Energy* **2017**, *2*, 17119; d) S. Choudhury, Z. Tu, S. Stalın, D. Vu, K. Fawole, D. Gunceler, R. Sundaraman, L. A. Archer, *Angew. Chem. Int. Ed.* **2017**, *56*, 13070; e) H. Ye, Z.-J. Zheng, H.-R. Yao, S.-C. Liu, T.-T. Zuo, X.-W. Wu, Y.-X. Yin, N.-W. Li, J.-J. Gu, F.-F. Cao, Y.-G. Guo, *Angew. Chem. Int. Ed.* **2019**, *58*, 1094; f) R. Wang, J. Yu, J. Tang, R. Meng, L. F. Nazar, L. Huang, X. Liang, *Energy Storage Mater.* **2020**, *32*, 178.

- [14] M. Zhu, B. Li, S. Li, Z. Du, Y. Gong, S. Yang, *Adv. Energy Mater.* **2018**, *8*, 1703505.
- [15] a) J. Wu, Z. Rao, X. Liu, Y. Shen, C. Fang, L. Yuan, Z. Li, W. Zhang, X. Xie, Y. Huang, *Adv. Mater.* **2021**, *33*, 2007428; b) L. Dong, L. Nie, W. Liu, *Adv. Mater.* **2020**, *32*, 1908494.
- [16] a) J. P. Perdew, K. Burke, M. Ernzerhof, *Phys. Rev. Lett.* **1996**, *77*, 3865; b) G. Kresse, J. Furthmüller, *Comp. Mater. Sci.* **1996**, *6*, 15.
- [17] Y. Xi, X. Ye, S. Duan, T. Li, J. Zhang, L. Jia, J. Yang, J. Wang, H. Liu, Q. Xiao, *J. Mater. Chem. A* **2020**, *8*, 14769.
- [18] H. Fan, Z. Zheng, L. Zhao, W. Li, J. Wang, M. Dai, Y. Zhao, J. Xiao, G. Wang, X. Ding, H. Xiao, J. Li, Y. Wu, Y. Zhang, *Adv. Funct. Mater.* **2019**, *30*, 1909370.
- [19] a) D. H. Youn, A. Heller, C. B. Mullins, *Chem. Mater.* **2016**, *28*, 1343; b) Z. Tu, S. Choudhury, M. J. Zachman, S. Wei, K. Zhang, L. F. Kourkoutis, L. A. Archer, *Nat. Energy* **2018**, *3*, 310.
- [20] J. Wang, S. Cheng, W. Li, L. Jia, Q. Xiao, Y. Hou, Z. Zheng, H. Li, S. Zhang, L. Zhou, M. Liu, H. Lin, Y. Zhang, *Nano Energy* **2017**, *40*, 390.
- [21] D. Lu, Y. Shao, T. Lozano, W. D. Bennett, G. L. Graff, B. Polzin, J. Zhang, M. H. Engelhard, N. T. Saenz, W. A. Henderson, P. Bhattacharya, J. Liu, J. Xiao, *Adv. Energy Mater.* **2015**, *5*, 1400993.
- [22] a) J. Wang, L. Jia, S. Duan, H. Liu, Q. Xiao, T. Li, H. Fan, K. Feng, J. Yang, Q. Wang, M. Liu, J. Zhong, W. Duan, H. Lin, Y. Zhang, *Energy Storage Mater.* **2020**, *28*, 375; b) S. Cheng, J. Wang, S. Duan, J. Zhang, Q. Wang, Y. Zhang, L. Li, H. Liu, Q. Xiao, H. Lin, *Chem. Eng. J.* **2021**, *417*, 128172.
- [23] a) W. Liu, S. W. Lee, D. Lin, F. Shi, S. Wang, A. D. Sendek, Y. Cui, *Nat. Energy* **2017**, *2*, 17035; b) L. G. Li, M. C. Wang, J. Wang, F. M. Ye, S. F. Wang, Y. A. Xu, J. Y. Liu, G. G. Xu, Y. Zhang, Y. Y. Zhang, C. Yan, N. V. Medhekar, M. N. Liu, Y. G. Zhang, *J. Mater. Chem. A* **2020**, *8*, 8033.
- [24] A. Basile, A. I. Bhatt, A. P. O'Mullane, *Nat. Commun.* **2016**, *7*, 11794.
- [25] J. Xiao, Q. Li, Y. Bi, M. Cai, B. Dunn, T. Glossmann, J. Liu, T. Osaka, R. Sugiura, B. Wu, J. Yang, J.-G. Zhang, M. S. Whittingham, *Nat. Energy* **2020**, *5*, 561.
- [26] a) Y. Xi, Q. Xiao, J. Du, X. Ye, X. Kong, Z. Chang, T. Li, H. Jin, J. Wang, H. Lin, *Adv. Mater. Interfaces* **2020**, *7*, 1902046; b) Q. Xiao, Y. Xi, J. Wang, D. Tu, W. You, X. Ye, H. Liu, X. Chen, H. Lin, *J. Phys. Chem. C* **2020**, *124*, 23086; c) C. Lu, Y. Yang, J. Wang, R. Fu, X. Zhao, L. Zhao, Y. Ming, Y. Hu, H. Lin, X. Tao, Y. Li, W. Chen, *Nat. Commun.* **2018**, *9*, 752.
- [27] T. Iwahashi, T. Miyamae, K. Kanai, K. Seki, D. Kim, Y. Ouchi, *J. Phys. Chem. B* **2008**, *112*, 11936.